Article

Sound field properties of non-cavitating marine propeller

Youjiang Wang *, Ulf Göttsche and Moustafa Abdel-Maksoud

Institute for Fluid Dynamics and Ship Theory (FDS), Hamburg University of Technology (TUHH), Am Schwarzenberg-Campus 4(C), 21073 Hamburg, Germany
* Correspondence: youjiang.wang@tuhh.de, wyg216@yeah.net; Tel.: +49-40-42878-6029.

Abstract: The sound field properties for non-cavitating marine propellers are studied using FW-H (Ffowcs William-Hawkings) acoustic analogy and BEM (Boundary Element Method) approach. For the first time, the FW-H formula to calculate acoustic pressure generated by the propeller wake sheet is proposed. The corresponding sound signal can be dominant up to several kilometres. Secondly, non-physical fictitious volume flux is observed when the permeable FW-H approach is used together with BEM. The reason is explained and a virtual source correction method is proposed to solve this problem. Furthermore, analytical analyse show that the second thickness term and the first two loading terms in Farassat 1A formula are important, and the others are negligible. The numerical studies show that the permeable FW-H approach produces underestimation when compared to the direct FW-H method, and the underestimation is severer for larger permeable surface and higher frequency. It is also found that the first loading term in Farassat 1A formula is the dominant source term in the direct FW-H method, while the first thickness term is dominant when the permeable FW-H approach is used.

Keywords: underwater radiated noise; propeller; Ffowcs William-Haukings; permeable FW-H; BEM

1. Introduction

The human-behaviour induced underwater noise has attracted public attention recently. It raises the underwater background noise level by a significant value [1] and very probably causes damage on marine life [2]. Shipping, or more exactly the operating marine propeller, is recognized as one of the main sources of the underwater radiated noise. Thus, different research projects are aimed to understand and reduce the radiated noise of marine propellers, e.g. the EU level projects AQUO, SONIC, and ProNoVi [3–5].

Numerical methods have already achieved popularity for the analysis of marine propeller hydrodynamics and for the design procedure. Also for problems related to underwater radiated noise, numerical simulations are expected to help to understand the mechanism and improve the design of marine propellers. Thus, appropriate simulations using different methods have been conducted in the last decade. Most of them have used the FW-H (Ffowcs William-Hawkings) acoustic analogy [6], more exactly the Farassat 1A formula given in [7], mostly due to its prevalence for investigating helicopter rotor noise. Ianniello et al. [8] have calculated the radiated noise of a complete scaled ship model using incompressible RANS simulation and the FW-H analogy. The direct volume integration and permeable FW-H approach were both used. For the direct volume integration, the averaged contribution of the turbulent fluctuating velocity components to the Lighthill stress was also included. Different permeable surfaces enveloping the whole ship were studied. Good correlation between the acoustic pressures and the RANS pressure signals were obtained. Lidtke et al. [9] used URANS and FW-H analogy to compute the tonal blade passage noise of the PPTC propeller

and used LES (Large Eddy Simulation) and FW-H analogy for the noise generated by a hydrofoil. The cavitation was also simulated using the Schnerr-Sauer model. It was concluded that RANS is unable to accurately account for cavitation dynamics and the associated noise. LES might help to gain detailed insight into the low-frequency noise generation mechanisms. It was also stated that the incompressibility assumption and the ignorance of fine-scale bubble dynamics would weaken the accuracy, and further refinement of the numerical methods was needed for more reliability. Li et al. [10] used DDES (Delayed Detached Eddy Simulation) and the permeable FW-H approach to compute the radiated noise of a full-scale ship and compared the results with sea trial measurements. The resulting pressure pulses were in close agreement with the measured ones at the first six orders of BPF (Blade Pass Frequency). Obvious underestimation of the broadband noise level in the frequency range 50-100Hz was identified, which was ascribed to the under-resolution of the tip vortex cavitation dynamics. Increasing underestimation of the noise level for frequency above 200Hz was also observed. Bensow and Liefvendahl [11] computed the radiated noise of a cavitating propeller operating behind a catamaran, more precisely, the research vessel Princess Royal, with using incompressible implicit LES and permeable FW-H approach. The results were compared with a model-scale measurement. The numerical results show a great underestimation in the low-frequency range up to around 400Hz, and a good agreement above 400Hz when compared to the measurements. Göttsche et al. [12] has also computed the Princess Royal case, but using the boundary element method together with FW-H analogy and compared the results with full-scale measurement. The ship hull was regarded as a sound source surface to consider the scattering effect. Reflections at the sea bed and the free surface were also considered. A general good agreement between the numerical results and the measurement was achieved. Also using potential-based panel method and FW-H formulation, Seol [13] has analysed the property of the sound field radiated by a marine propeller without cavitation and with sheet cavitation. For the non-cavitating case, a clear dipole directivity pattern was identified. When sheet cavitation occurs, it becomes the dominant noise source.

Due to the complex operating situation of the marine propellers and different properties of the fluid field compared to aerodynamics, e.g. the ship wake field and the cavitation phenomenon, the early-stage simulations were not found satisfactory. There were different kinds of deviations between simulations and measurements. Therefore, marine researchers have dug more deeply into the acoustic theory, and tried to obtain a better understanding and appropriate usage of acoustic analogies. Ianniello [14] developed a concept of rot-pole for the analytical study of rotating sound sources. The properties of the resulting sound field have been analysed, including the dependence of the decay rate on the Mach number and the number of source points, which is a representation of the propeller blade number. It was found that the decay rate out of the rotating disk plane is one order faster than in the disk plane. In the disk plane, the decay rate is firstly r^{-2} in the near-field and then r^{-1} in the far-field. Increasing the number of source points leaded to a faster decay rate in the near-field, but did not influence the property in the far-field. Cianferra [15] has derived a numerically applicable formula for the volume integration of the quadrupole term in the FW-H equation. With the flow field obtained using LES, he compared the acoustic results obtained by direct volume integration method and multiple permeable FW-H approaches for the flow-generated sound from a square cylinder. It was concluded that the direct integration method gave the most accurate results and the computational effort was acceptable. Further comparative analysis also showed that the persistence of a 2D shaped wake produced more radiated noise when compared to a 3D wake. Leifvendahl and Bensow [16] have studied the flow-generated sound from different cylinders with both numerical simulation and semi-empirical model. For the numerical simulation, LES and Curle acoustic analogy were used. LES was also used to determine the parameters for the semi-empirical model. In-depth analysis of the cylinder flow regarding the sound generation was conducted, e.g. the spanwise correlation of the vortex structures. The resulting sound predictions showed reasonable agreement with measurements.

In this work, the sound field property of non-cavitating marine propellers is studied using the FW-H equation and the BEM (Boundary Element Method) approach. The decay rates and the

relative importance of different terms in the FW-H equation at various distances will be shown. The investigation is conducted both for the propeller working in uniform flow field (open water case) and in the ship wake field (unsteady case). The distance covers the range from less than one propeller diameter up to several acoustic wavelengths. The formula to consider acoustic pressure induced by the potential wake sheet, which models the vorticity flow after the propeller, is given for the first time. The property and relative importance of the blade surface and wake flow induced acoustic pressures are analysed. The permeable FW-H approach is also studied, including comparison with the direct FW-H method and the influence of the permeable surface size on acoustic results.

Although BEM is unable to capture so much flow details as the finite volume CFD methods, e.g. RANS, DES or LES. But BEM has advantages over these methods to study the property of FW-H equation and the permeable FW-H approach. There is no information loss between the permeable surface and the blade surface caused by numerical diffusion. There is also no vorticity distribution in the flow field, which requires a volume integration for the accurate acoustic calculation. Besides, without numerical diffusion, the pressure distribution obtained with the Bernoulli equation corresponds exactly to the flow field solution. Although it is the result with the assumption of incompressibility (or infinite sound speed), such a pressure distribution can still supply a 'gauge' to compare with.

During the study, it would be shown that the radiated noises of open water and unsteady cases have quite different properties. It is also found that some popular or even canonical numerical treatments in BEM, which are justified for calculating hydrodynamic forces, would have an obvious influence on the acoustic pressure.

The rest of the manuscript is organized as follows. The mathematical formulas, term definitions, and important numerical methods are described in section 2. In section 3 an analysis of the order of magnitude for the FW-H terms are presented, which give a rough idea which terms would be important or secondary for the marine propeller problem. Then numerical results for different cases and the corresponding analysis are given in section 4. Finally, the conclusions are summarized in section 5.

2. Methodology

In the current work, the locations of the observer points are constant relative to the ship, i.e. they move forward together with the propeller. Although this set-up may not be consistent with full-scale experiment, this is a popular treatment in numerical simulations.

A very simple description of BEM is given firstly in section 2.1, to help understand the treatment of FW-H equation in BEM better. Then the used FW-H formulas are given or derived in sections 2.2 to 2.4.

2.1. Boundary element method

In BEM the flow is assumed to be inviscid and irrotational. Thus, the potential theory is used and the main unknown is the disturbed velocity potential ϕ. Knowing its values and normal derivatives on the boundaries are enough to give a deterministic distribution of ϕ in the fluid domain. The potential's jump (equivalent to potential value when ϕ is assumed to be zero inside the body) and normal derivative are represented by doublet and source strength on the boundaries, and they are the variables to be solved for. The domain boundaries consist of the solid body boundary and the wake sheet. The wake sheet geometry is determined through an iterative process called wake alignment, which requires the wake sheet being locally tangent to the fluid velocity. The boundaries are discretized into panels to enable a numerical solution, as shown in Figure 1. There are source and doublet on the solid body panels and only doublet on the wake panels. They induce potentials and velocities in the fluid domain. In current work, our in-house low order BEM code *pan*MARE is used, which means the source and dipole strength are constant on the panel.
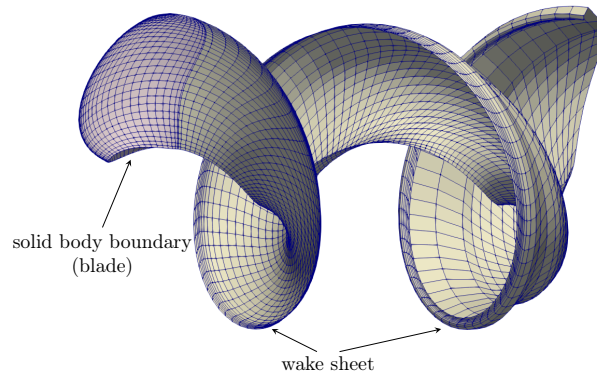
Figure 1. The surfaces and discretization in the boundary element method. Courtesy to [17].

In steady cases, the doublet strengths are constant on each streamwise wake panel strip and are determined according to Kutta condition [18]. In unsteady cases, the doublet strength changes along the streamwise direction due to the time-varying load on the blades. In the current work, the source strengths are pre-evaluated according to impermeable condition (zero normal velocity on the body surface), the doublet strengths are obtained by solving a system of linear equations built with the Dirichlet boundary condition. Knowing the source and doublet strengths, the velocity distribution can be obtained by adding up the induced velocities and the undisturbed inflow. The pressure in the fluid domain is calculated with the unsteady Bernoulli equation.

More detailed descriptions of BEM can be found in [18–20].

2.2. Ffowcs Williams-Haukings equation

The current work is based on the FW-H equation in the Farassat 1A form [7], which is

$$p'(\boldsymbol{x}, t) = p'_T(\boldsymbol{x}, t) + p'_L(\boldsymbol{x}, t) \tag{1}$$

$$
4\pi p'_T(\boldsymbol{x}, t) = \int_{f=0} \left[\frac{\rho_0 \left(\dot{U}_n + U_{\dot{n}} \right)}{r \left(1 - M_r \right)^2} \right]_{\mathrm{ret}} dS \\
+ \int_{f=0} \left[\frac{\rho_0 U_n \left\{ r \dot{M}_r + c_0 \left(M_r - M^2 \right) \right\}}{r^2 \left(1 - M_r \right)^3} \right]_{\mathrm{ret}} dS \tag{2}
$$

$$
4\pi p'_L(\boldsymbol{x}, t) = \frac{1}{c_0} \int_{f=0} \left[\frac{\dot{L}_r}{r \left(1 - M_r \right)^2} \right]_{\mathrm{ret}} dS \\
+ \int_{f=0} \left[\frac{L_r - L_M}{r^2 \left(1 - M_r \right)^2} \right]_{\mathrm{ret}} dS \\
+ \frac{1}{c_0} \int_{f=0} \left[\frac{L_r \left\{ r \dot{M}_r + c_0 \left(M_r - M^2 \right) \right\}}{r^2 \left(1 - M_r \right)^3} \right]_{\mathrm{ret}} dS \tag{3}
$$

$$\boldsymbol{U} = \boldsymbol{v} + \frac{\rho}{\rho_0} \left(\boldsymbol{u} - \boldsymbol{v} \right) \tag{4}$$

$$\boldsymbol{L} = p\boldsymbol{n} + \rho \boldsymbol{u}(u_n - v_n) \tag{5}$$

where $p'(\boldsymbol{x}, t)$ is the sound pressure at the observer position $\boldsymbol{x}$ and time point t, p'_T and p'_L are called the thickness and loading terms, respectively; $f = 0$ denotes the integration surface for FW-H equation (or sound source surface), ρ is the fluid density, ρ_0 is the undisturbed value, c_0 is the sound speed, and

145 p is the absolute pressure; u is the fluid velocity, v is the surface moving velocity, both are defined in a
146 coordinate where the undisturbed fluid (or far-field fluid) is static; M is the vectorial Mach number, i.e.
147 $M = v/c_0$; r is the vector from the source point to observer position, r is its length, the subscript ret
148 means that variables inside the square brackets are computed at the corresponding retarded times, i.e.
149 at $\tau = t - r/c_0$; the subscripted variables denote dot products of a vector and a unit vector implied by
150 the subscript, except for $L_M = L \cdot M$, and n is the unit normal vector on the surface directing into the
151 fluid domain; the dot over a variable means time derivative.

In equation (1) the quadrupole component due to the Lighthill stress tensor is ignored, because it
vanishes in an incompressible potential fluid domain. As the observer is moving relative to the static
fluid, the position change between the retarded time τ and the observer time t must be considered.
This is done by calculating the vector r using the formula provided by Bres et al. [21], i.e.

$$r = \left(\frac{\Delta x + M_0 \sqrt{\Delta x^2 + \beta^2 (\Delta y^2 + \Delta z^2)}}{\beta^2}, \Delta y, \Delta z \right) \tag{6}$$

with

$$\beta = \sqrt{1 - M_0^2} \tag{7}$$

and

$$M_0 = \frac{u_0}{c_0} \tag{8}$$

152 where Δx, Δy and Δz are components of the vector from source point to the observer position at the
153 retarded time, and u_0 is the observer's velocity along the x direction. The motion in other directions
154 would not be considered in the current study. Normally, the global coordinate can be chosen to meet
155 this motion direction requirement.

To facilitate the detailed analysis of the components, the thickness and loading terms given in
equations (2) and (3) are further decomposed as

$$p'_T = p'_{T,1} + p'_{T,2} = p'_{T,1} + (p'_{T,2-1} + p'_{T,2-2}) \tag{9}$$

$$p'_L = p'_{L,1} + p'_{L,2} + p'_{L,3} \tag{10}$$

where

$$4\pi p'_{T,1} = \int_{f=0} \left[\frac{\rho_0 \left(\dot{U}_n + U_{\dot{n}} \right)}{r \left(1 - M_r \right)^2} \right]_{\text{ret}} dS \tag{11}$$

$$4\pi p'_{T,2-1} = \int_{f=0} \left[\frac{\rho_0 U_n \dot{M}_r}{r \left(1 - M_r \right)^3} \right]_{\text{ret}} dS \tag{12}$$

$$4\pi p'_{T,2-2} = \int_{f=0} \left[\frac{\rho_0 U_n c_0 \left(M_r - M^2 \right)}{r^2 \left(1 - M_r \right)^3} \right]_{\text{ret}} dS \tag{13}$$

$$4\pi p'_{L,1} = \frac{1}{c_0} \int_{f=0} \left[\frac{\dot{L}_r}{r \left(1 - M_r \right)^2} \right]_{\text{ret}} dS \tag{14}$$

$$4\pi p'_{L,2} = \int_{f=0} \left[\frac{L_r - L_M}{r^2 \left(1 - M_r \right)^2} \right]_{\text{ret}} dS \tag{15}$$

$$4\pi p'_{L,3} = \frac{1}{c_0} \int_{f=0} \left[\frac{L_r \left\{ r \dot{M}_r + c_0 \left(M_r - M^2 \right) \right\}}{r^2 \left(1 - M_r \right)^3} \right]_{\text{ret}} dS \tag{16}$$

On the solid surface, the impermeable condition implies $u_n = v_n$. Thus the term U_n and L on the solid surface can be simplified to

$$U_n = v_n \tag{17}$$

$$L = p\boldsymbol{n} \tag{18}$$

2.3. FW-H equation on the potential wake sheet

In BEM, the wake sheet is used to represent the shedding vorticity of the blades. The wake sheet has zero thickness and acts as a potential boundary in the solution process, as shown in Figure 1. In this section, we will show that the zero-thickness surface representation of the vorticity field turns the volume integration of the Lighthill stress term into a surface integration on the wake sheet.

The evolution of the wake sheet can be considered in two perspectives, or two coordinate reference systems, i.e. the earth-fixed global reference system and the propeller-fixed local reference system. To make the problem simple, the wake alignment is not considered in the derivation. In the earth-fixed perspective, the propeller rotates and moves forward, and new wake panels are shed out at the trailing edge in every time step. The existing wake panels are static and the doublet strengths on them do not change with time. The wake panels being far enough from the blade are removed to reduce computational cost and mimic the vorticity diffusion. Normally a wake length will be defined to limit the maximum wake panel numbers in the streamwise direction. In the propeller-fixed perspective, both the propeller and the wake panels stay static. The doublet strength is convected panel-wise downstream. Therefore, the doublet strength on the wake panel is time-varying. These two perspectives are depicted in Figure 2.
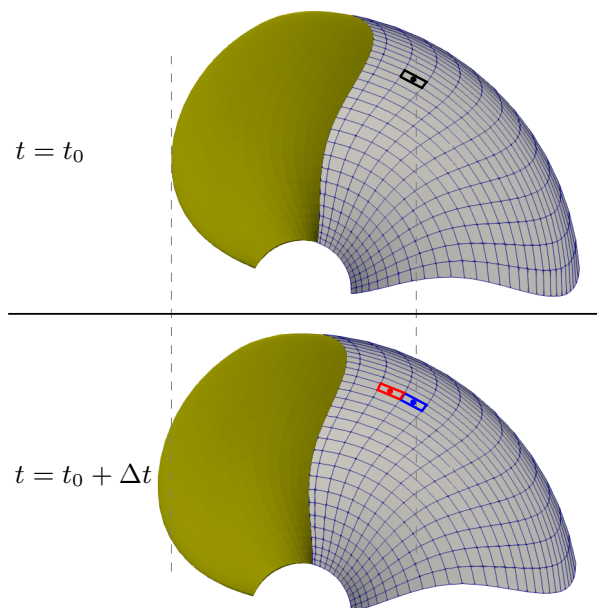

Figure 2. Different perspectives to consider the evolution of wake sheet. For the selected black panel in the current time step. The same panel in the next time step would be the blue one in the earth-fixed perspective, and the red one in the propeller-fixed perspective.
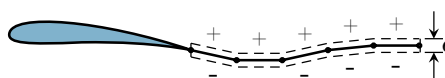

Figure 3. The FW-H integration surfaces enveloping the wake sheet. The gap between the upper and lower surface ϵ is set to be infinitely close to zero.

172   Now we derive the FW-H equation on the wake sheet in the propeller-fixed perspective. A closed
173 surface is used to envelop the wake sheet. The surface consists of two subsurfaces parallel to the wake
174 sheet, i.e. the upper subsurface and the lower subsurface on both side, and end cap subsurfaces to
175 close the envelope, as shown in Figure 3. Let the distances between the two parallel subsurfaces to the
176 wake sheet approach zero, then they have the same position with the wake sheet and normal directions
177 opposite to each other. The areas of the end cap surfaces become zero and their contribution to the
178 acoustic pressure vanishes.

179   We now discrete the upper and lower subsurfaces in the same manner with the wake sheet. Then
180 every FW-H term will be checked on the panel. It will be shown that thickness terms cancel out each
181 other, while the loading terms do not totally vanish and form the FW-H formula on the wake sheet.
182 We use the superscript '+' to denote the variable values on the upper subsurface and '-' for those on
183 the lower subsurface, no superscript means the summed effect.

184 2.3.1. Thickness terms

Because there is no potential source on the wake sheet, so the normal component of the fluid
velocity is equal on the upper and lower subsurfaces. Due to the opposite normal directions, the
following relationship holds:

$$u_n^+ + u_n^- = 0.$$

Because the upper and lower subsurfaces share the same position with the wake sheet, the surface
moving velocities are the same, i.e.

$$v^+ = v^-.$$

With these two relationships, the following results can be deduced

$$U_n = U_n^+ + U_n^- \equiv 0 \tag{19}$$

and

$$\dot{U}_n + U_{\dot{n}} = dU_n/dt \equiv 0. \tag{20}$$

These imply further that on the wake sheet

$$p_T' = p_{T,1}' = p_{T,2}' = 0 \tag{21}$$

185 2.3.2. loading terms

With the above-mentioned velocity relation, the following equation can be obtained

$$\boldsymbol{L} = (p^+ - p^-)\boldsymbol{n} + \rho(\boldsymbol{u}^+ - \boldsymbol{u}^-)(u_n - v_n) \tag{22}$$

For the first term on the right-hand side, the pressure is calculated with the unsteady Bernoulli
equation, i.e.

$$p = \rho_0 \left[\frac{1}{2}U_\infty^2 - \frac{1}{2}(\boldsymbol{U}_\infty + \boldsymbol{u}_{ind})^2 - \frac{d\phi}{dt} \right] + p_0 \tag{23}$$

where $\boldsymbol{U}_\infty$ is the undisturbed relative inflow velocity, $\boldsymbol{u}_{ind}$ is the induced velocity, ϕ is the perturbation
velocity potential, and p_0 is the far-field pressure. With the unsteady Bernoulli equation, it can be
obtained that

$$p^+ - p^- = \rho_0 \left[\left(\boldsymbol{U}_\infty + \frac{\boldsymbol{u}_{ind}^+ + \boldsymbol{u}_{ind}^-}{2} \right) \cdot (\boldsymbol{u}_{ind}^+ - \boldsymbol{u}_{ind}^-) - \frac{d(\phi^+ - \phi^-)}{dt} \right] \tag{24}$$

The difference $(\boldsymbol{u}_{ind}^{+} - \boldsymbol{u}_{ind}^{-})$ is related to the vortex density on the surface. It is zero on the wake panels in a lower order BEM code. Considering the relationship between doublet strength and potential jump on the wake panel, i.e. $-\mu = (\phi^{+} - \phi^{-})$, we have

$$p^{+} - p^{-} = \rho \frac{d\mu}{dt} = \rho \dot{\mu} \tag{25}$$

For the second term on the right-hand side of equation (22), the difference $(\boldsymbol{u}^{+} - \boldsymbol{u}^{-})$ is related to the vortex density on the surface, which is zero on the wake panels in a lower order BEM code. Thus, the second term would vanish.

Combination of these two terms leads to

$$\boldsymbol{L} = \rho \dot{\mu} \boldsymbol{n}. \tag{26}$$

This can be substituted into equations (14) to (16) for the calculation of acoustic pressures. In the open water case, $\dot{\mu} \equiv 0$, thus the wake sheet does not contribute to the acoustic pressure. For the unsteady case, the term does not vanish and will generate acoustic pressure.

The numerical results will show that the term $p'_{L,1}$ is dominant among the wake sheet induced acoustic pressure. To enable a further detailed analysis, the term $p'_{L,1}$ is separated further to $p'_{L,1-1}$ and $p'_{L,1-2}$, i.e.

$$4\pi p'_{L,1-1} = \frac{1}{c_0} \int_{f=0} \left[\frac{\rho_0 (\dot{\mu} \dot{n})_r}{r (1 - M_r)^2} \right]_{ret} dS \tag{27}$$

$$4\pi p'_{L,1-2} = \frac{1}{c_0} \int_{f=0} \left[\frac{\rho_0 (\dot{\mu} n)_r}{r (1 - M_r)^2} \right]_{ret} dS \tag{28}$$

In the earth-fixed perspective, because of non-time-varying doublet strength on the wake panels, the same analysis will lead to zero loading terms. However, there is a dilemma about the newly generated wake panels. It implies a local growth of the integration surface, for which the Farassat 1A formulas are invalid, because the surface divergence term in the original work of Ffowcs Williams and Hawkings [6, equation 4.3] has been ignored or regarded as unity. When the focus is put locally on the newly generated wake panels, the area of the integration surface grows from zero to a finite value, which means an infinite surface divergence. Then the integration on the new panels is undefined. Such a dilemma does not happen in the propeller-fixed perspective.

2.4. Permeable FW-H approach with BEM

When a permeable surface enveloping the propeller and wake sheet is used, the equations (1) to (8) can be applied without any modification. Normally the permeable surface moves forward together with the propeller. All quantities should be defined in the static flow, thus $\boldsymbol{u}$ is the fluid velocity in the earth-fixed reference coordinate system, and $\boldsymbol{v}$ is the constant forward velocity.

In the potential solver, the first problem for the permeable FW-H approach is whether the ship wake velocity should be considered in $\boldsymbol{u}$. If so, how it should be included. Normally, ship wake velocities are only provided on the propeller disk. This information is not enough to obtain the ship wake velocity on the whole permeable surface due to its large dimensions in both the radial and axial directions. At the same time, because of the nonlinear relation between pressure and local fluid velocity, the addition of even a constant ship wake velocity will result in differences of all the loading terms. The second thickness term $p'_{T,2}$ is also influenced. The first thickness term is an exception. If we choose the permeable surface so that the normal vectors on the surface do not change with time, then $U_{\dot{n}}$ will not be influenced. If the ship wake velocity is timely constant, which is a canonical assumption in the potential solver, then $\dot{U}_n$ is also not influenced. Thus, under the two above mentioned conditions, the term $p'_{T,1}$ keeps the same when the ship wake velocity is included or ignored on the permeable surface. It will be shown in section 4.3 that the $p'_{T,1}$ is, fortunately, the dominant term when the FW-H

217 permeable formula is used. Thus it becomes unimportant whether to include the ship wake velocity in
218 u.

219   The second problem is caused by the use of 2D ship wake velocity information as a 3D velocity
220 field. This results in a non-divergence-free velocity field. The potential source on the blade surface,
221 which is calculated according to this velocity field, would therefore not integrate to zero. This will
222 be manifested by a non-negligible volume flux on the permeable surface. This fictitious volume
223 flux depends on the propeller's azimuthal position and is thus time-varying. It will generate pure
224 numerical acoustic pressures and contaminate the results. A simple but effective solution is adding a
225 virtual source point at the propeller centre to cancel out the fictitious volume flux. The integral source
226 strength on the propeller surface is calculated in every time step, and its opposite is used to set the
227 strength of the virtual source point. Then the induced velocity of the virtual source point is superposed
228 on existing velocities on the permeable surface. Such a virtual source correction procedure ensures a
229 significant reduction of the fictitious volume flux.

230 **3. Order of magnitude analysis**

    In this section, we conduct a rough mathematical analysis for the orders of magnitude of the FW-H
terms on the blade surfaces. Without loss of generality, the propeller's rotation and forward speed are
assumed to be constant, and the propeller is regarded as a rigid body. Under these assumptions, the
normal surface motion velocity v_n do not change with time, i.e.

$$\frac{dv_n}{dt} \equiv 0 \tag{29}$$

231   Before the formal analysis, two concepts are introduced, i.e. the far-field term and the near-field
232 term, which have the decay rates of r^{-1} and r^{-2}, respectively. It is obvious that with enough distance,
233 i.e. in the far-field, the far-field terms are dominant over the near-field terms.

234   During the analysis, when concrete values are needed, the corresponding parameters of the KP505
235 propeller are taken as references. KP505 is an open access five-blade fixed pitch propeller designed
236 for the MOERI container ship (KCS) [22], and its main particulars are listed in table 1. Other cases
237 should not have large differences regarding orders of magnitude of the parameters. For the analysis,
238 $|M| = |v/c_0| << 1$ is assumed, which is valid for most marine propeller cases.

Table 1. Principal particulars for the KP505 propeller.

parameter	symbol	value
diameter	D	7.9m
number of blades	Z	5
designed advance ratio	J_0	0.7
rotation rate	n	1.25s^{-1}
angular speed	ω	7.85s^{-1}
BPF (Blade Pass Frequency)	f_1	6.25Hz
acoustic wave length for BPF	λ_1	240m

For the first thickness term $p'_{T,1}$, we have

$$\dot{U}_n + U_{\dot{n}} = \frac{dU_n}{dt} = \frac{dv_n}{dt} = 0,$$

which means

$$p'_{T,1} \equiv 0 \tag{30}$$

Furthermore, the following proportional relations exist

$$U_n = v_n \propto \omega D, \quad |\dot{v}| \propto v\omega, \quad |\dot{M}| \propto v\omega/c_0 \propto \omega^2 D/c_0,$$

where D is the propeller diameter, v is the magnitude of $\boldsymbol{v}$, and ω is the rotation speed. Together with the condition $M_r << 1$, and considering the integrand of $p'_{T,2-1}$ in equation (12), i.e.

$$\frac{\rho_0 U_n \dot{M}_r}{r\left(1-M_r\right)^3},$$

it can be obtained that

$$p'_{T,2-1} \propto \frac{\rho_0 \omega^3 D^2}{r c_0} \tag{31}$$

With the same procedure, the proportional relation for $p'_{T,2-2}$ can be expressed as

$$p'_{T,2-2} \propto \frac{\rho_0 \omega^2 D^2}{r^2} \tag{32}$$

Then, for the loading terms, the following relations are used

$$p \propto \rho_0(\omega D)^2, \quad \dot{p} = \omega \frac{dp}{d\theta} \propto \rho_0 \omega^3 D^2, \quad |\dot{\boldsymbol{n}}| \propto \omega,$$

$$L \propto p, \quad |\dot{L}| = |\dot{p}_n + p_{\dot{n}}| \propto \rho_0 \omega^3 D^2, \quad L_M << L_r$$

where θ is the azimuthal angle. Using these relations we obtain

$$p'_{L,1} \propto \frac{\rho_0 \omega^3 D^2}{r c_0} \tag{33}$$

$$p'_{L,2} \propto \frac{\rho_0 \omega^2 D^2}{r^2} \tag{34}$$

$$p'_{L,3} \propto \frac{\rho_0 \omega^4 D^3}{r c_0^2} + \frac{\rho_0 \omega^3 D^3}{r^2 c_0} \tag{35}$$

239 With these proportional relations in equations (31) to (35), some insights into the relative
240 significance of the FW-H terms can be achieved. Firstly, considering the situation where $\omega D/c_0 \propto$
241 $M << 1$, it can be concluded that $p'_{L,3}$ is always secondary when compared to $p'_{L,1} + p'_{L,2}$ for the
242 marine propeller problem. Then, only four terms remain to be investigated, which are $p'_{T,2-1}$, $p'_{T,2-2}$,
243 $p'_{L,1}$, and $p'_{L,2}$.

It can be observed that $p'_{T,2-1}$ and $p'_{L,1}$ are far-field terms and $p'_{T,2-2}$ and $p'_{L,2}$ are near-field terms. Besides, $p'_{T,2-1}$ and $p'_{L,1}$ are proportional to the same kernels, and the terms $p'_{T,2-2}$ and $p'_{L,2}$ also. If $p'_{T,2-1}$ and $p'_{L,1}$ are compared using their original integrands in equations (12) and (14), it turns out to be the comparison

$$\rho_0 v^2 \quad \text{vs.} \quad p + dp/d\theta.$$

For the near-field terms $p'_{T,2-2}$ and $p'_{L,2}$ it would be the comparison

$$\rho_0 v^2 \quad \text{vs.} \quad p.$$

244 Taking the KP505 propeller as an example, the surface motion velocity v is around 30m/s near the
245 tip, and $\rho_0 v^2$ approaches the order of magnitude 10^6. For a ship propeller, p is in the same order of
246 magnitude with the atmospheric pressure, i.e. 1×10^5 ~2×10^5. For vehicles working in deep water,
247 p would have a different order of magnitude. The term $dp/d\theta$ is quite small for open water case
248 and smaller than p when ship wake field is smooth, but can also achieve the order of 10^5 when the
249 propeller works in a severe ship wake field. Thus, the thickness terms $p'_{T,2-1}$ and $p'_{T,2-2}$ seem to be
250 more significant than the loading terms $p'_{L,1}$ and $p'_{L,2}$, with integrands having one order higher of

251   magnitude. The numerical results in section 4.1 will show that it is really the case for the open water
252   case.

253   However, in unsteady cases, the motion velocity has the same value on different blades, while
254   p and $dp/d\theta$ are highly θ-dependent. The interference then leads to a much faster decay rate of the
255   thickness terms than that of the loading terms. This result in the dominance of the loading terms over
256   the thickness terms in unsteady cases.

257   When comparison are conducted between the near-field and far-field terms, i.e. between $p'_{T,2-1}$ in
258   (31) and $p'_{T,2-2}$ in (32) or between $p'_{L,1}$ in (33) and $p'_{L,2}$ in (34), it can be found that the distance where
259   the dominant term changes is related to $c_0/\omega = \lambda_1/(2\pi Z)$, where λ_1 is the acoustic wavelength for
260   the 1st BPF. However, this formula can not directly be used to calculate the critical distance. Other
261   factors, e.g. the interference, must be considered.

4. Numerical Results

263   To study the decaying behaviour and determine the dominant FW-H term at different distances, a
264   set of observer points are placed in the propeller disk plane. They are located on the right side of the
265   propeller and the distances to the propeller centre are from 5m to 550m, which is around 70D or $2.3\lambda_1$.
266   The numerical result will be presented mainly for the 1st BPF.

4.1. Open water case

268   The full-scale KP505 case is calculated at the design point. The obtained sound pressure level
269   for the BPF is given in Figure 4. One is calculated with FW-H equation, the other is calculated
270   with the Bernoulli equation using the velocities and potential obtained in the BEM solver. The SP
271   (Sound Pressure) obtained with FW-H decays very fast, i.e. with the rate of $r^{-(1+Z)}$ in the near-field.
272   Then beyond 100m, the decay rate gradually changes to r^{-1}. The pressure oscillation amplitudes
273   correlate very well with those obtained with Bernoulli equation in the near-field. However, the
274   Bernoulli pressure signal decays always with the rate $r^{-(1+Z)}$, which is due to the infinite sound speed
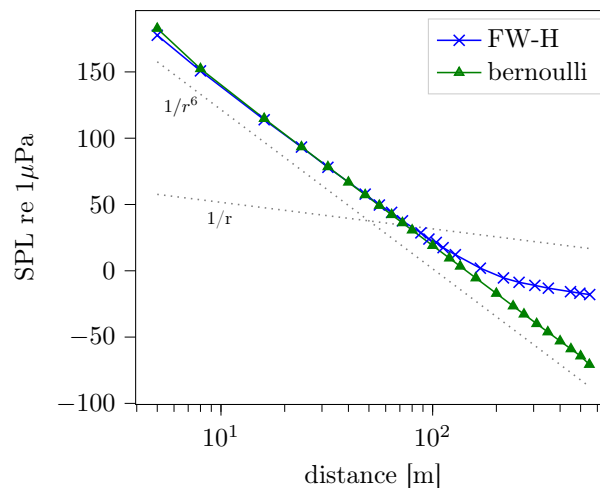275   assumption in the BEM solver. This leads to the deviation in the far-field.

Figure 4. Sound pressure level obtained with different methods for the open water case.

276   Figure 5 shows the contributions of different FW-H terms. For the open water case, the thickness
277   terms are always dominant over the loading terms. The thickness term $p'_{T,2-2}$ is dominant in the
278   near-field and $p'_{T,2-1}$ is dominant in the far-field, which is in agreement with the analytical analysis in
279   section 3. The change of the dominant role happens around 200m, which is 25D or 0.85λ.

280   It can also be observed that, the far-field terms $p'_{T,2-1}$, $p'_{L,1}$, and $p'_{L,3}$ decay with the decay rate
281   r^{-Z} in the near-field and r^{-1} in the far-field. The near-field terms $p'_{T,2-2}$ and $p'_{L,2}$ decays with the
282   rate $r^{-(1+Z)}$ in the near-field and r^{-2} in the far-field. That means the decay rate is increased in the

near-field due to the interference between acoustic pressures from different blades . The transition of the decay rate happens in the range from 100m to 300m.
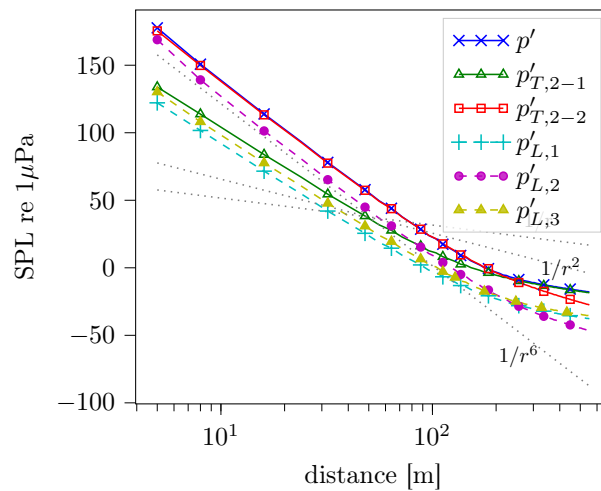

Figure 5. Contribution of different FW-H terms for open water case.

The results for the open water case agree very well with the analytical in-plane decay behaviour of the rot-pole, i.e. a sound source consisting of one or more rotating force sources, which is proposed and analysed by Ianniello [14]. Figure 24 and 27 in [14] show a decay rate of $r^{-(1+Z)}$ in the near-field and r^{-1} in the far-field for both the total thickness term and total loading term. This is the combined effect of the behaviours of all the terms shown in Figure 5 here.

4.2. Unsteady case

For the unsteady case, the propeller operates in a ship wake field. The used ship wake field is shown in Figure 6. It is a relatively smooth wake field with a wake fraction of $w = 0.16$. The propeller advancing speed V_s is set to make the effective advance ratio being $\frac{(1-w)V_s}{nD} = 0.7$.
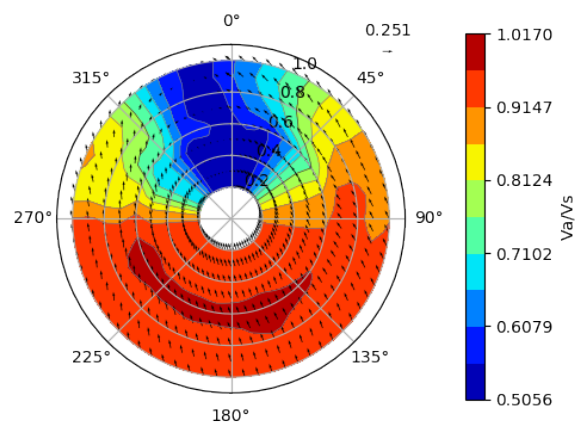
Figure 6. The ship wake field used for current work.

The sound pressure level obtained with different propeller wake sheet lengths are given in Figure 7, in the form of separate contributions from blade surface, wake sheet and combined results. There is no obvious range in which the SP decays very fast, i.e. with the rate $r^{-(1+Z)}$ as for the open water case. The blade induced SP correlates very well with the results obtained with the Bernoulli equation. They both decay with a rate between r^{-2} and r^{-1} beyond 20m. Such a good correlation does not mean that the wake sheet contribution is not justified. Later we will see that the dominant FW-H term on

the wake sheet has a close relation to the finite sound speed, which is not captured in the Bernoulli pressure signal.

The wake sheet induced SPL increases with the wake sheet length. For short wake sheet lengths, i.e. 1 and 2 revolutions, the blade induced SPL is dominant. For long wakes, i.e. no less than 3 revolutions, the wake sheet induced SPL is dominant in a large distance rage (< 400m for 3 revolutions). The wake sheet induced SP has a decay rate of r^{-2}, which is faster than that of the blade induced SP. This implies that the blade would always be the dominant role in the very far field, but the distances might need to be larger than several kilometres. Figure 8 shows the variation of the SPL up to 4km for the cases with 2 and 3 wake revolutions. With 3 wake revolutions, the wake sheet induced SPL crosses the blade induced SPL around 700m and the wake sheet effect can be ignored firstly at the distance around 3km.
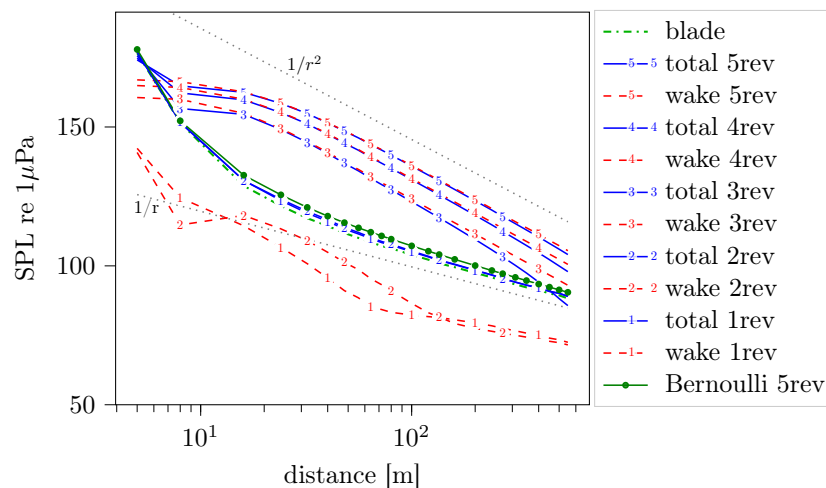
Figure 7. Sound pressure levels for the unsteady case calculated with different wake sheet lengths. In the legend *blade* means only FW-H terms on the blade, *wake* means only FW-H terms on the wake sheet, *total* means the combination of both. 1rev ~5rev denote the length of wake sheet in revolutions.
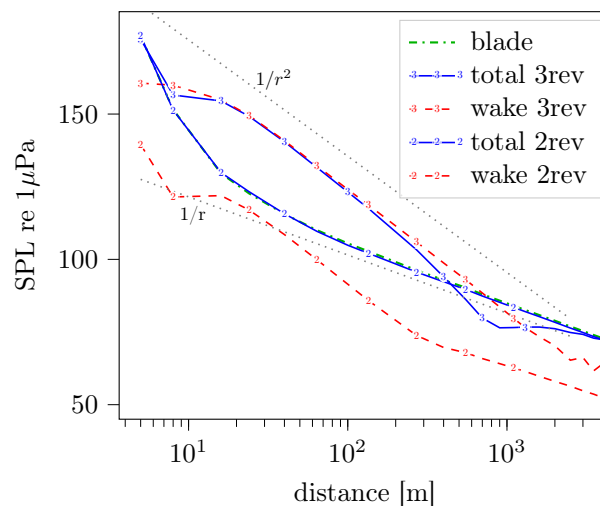

Figure 8. Comparison of the results with 2 and 3 wake revolutions for a long distance range. In the legend *blade* means only FW-H terms on the blade, *wake* means only FW-H terms on the wake sheet, *total* means the combination of both. 2rev and 3rev denote the length of wake sheet in revolutions.

Figure 9 shows the contributions of different FW-H terms in the blade induced SPL. In the unsteady case, the thickness terms are no longer dominant due to the slower decay rates of the loading terms. The terms $p'_{L,1}$ and $p'_{L,2}$ dominate the SPL in the far-field and near-field relatively, and the transition happens around 40m (5D). The transition position should, however, be case-dependent.

³¹⁴ Unlike in the open water case, in the unsteady case $p'_{L,1}$ and $p'_{L,2}$ achieve the final decay rates of r^{-1}
³¹⁵ and r^{-2} quite early, i.e. at the distance around 16m (2D). The reason is that the pressure and also the
³¹⁶ time derivative of pressure are not equal on each blade, which is caused by the inhomogeneous ship
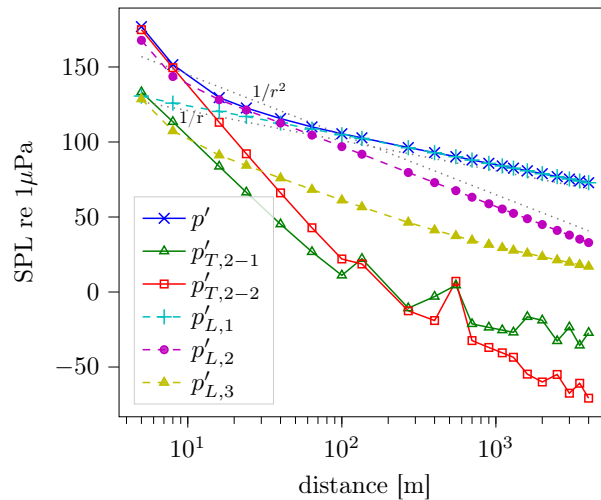³¹⁷ wake field. Therefore the interference effect becomes quite weak.

Figure 9. Contributions of different FW-H terms in the blade induced SPL. The oscillation of the thickness terms are due to interferences.

³¹⁸ Figure 10 shows the contributions of different FW-H terms in the wake sheet induced SPL, for
³¹⁹ both cases with 2 and 3 wake revolutions. The thickness terms are always zero and are therefore not
³²⁰ shown. Beyond 40m (5D), the dominant term is $p'_{L,1}$, more exactly $p'_{L,1-2}$, which is defined in equation
³²¹ (28). Beyond 5D the decay rate of $p'_{L,1-2}$ is firstly r^{-2} and then changes to r^{-1} at a position, which is
³²² dependent on the wake sheet length. The term $p'_{L,1-1}$ decays always with the rate r^{-1} beyond 5D. In
³²³ the both cases, $p'_{L,1-2}$ achieves the decay rate of r^{-1} before it becomes smaller than $p'_{L,1-1}$. Thus the
³²⁴ dominant term beyond 5D is always $p'_{L,1-2}$.
³²⁵ According to equation (14), the term $p'_{L,1}$, including both $p'_{L,1-1}$ and $p'_{L,1-2}$, is inversely
³²⁶ proportional to the sound speed. An infinite sound speed assumption would make these terms
³²⁷ vanish. This explains the difference between the Bernoulli pressure signal and the acoustic pressure
³²⁸ obtained with both blade and wake sheet in Figure 7.
³²⁹ One possible explanation for the dominance of $p'_{L,1-2}$ over $p'_{L,1-1}$ could be the relative smoothness
³³⁰ of currently used ship wake field. According to the equation (27), $p'_{L,1-1} \propto \ddot{u}$, and $\ddot{u}$ is related to the
³³¹ second azimuthal derivative of the velocity in ship wake field. According to the equation (28),
³³² $p'_{L,1-2} \propto |\dot{u}\dot{n}|$, and $\dot{u}$ is related to the first azimuthal derivative of the velocity in ship wake field. With
³³³ a smooth ship wake field, the second azimuthal derivative of velocity would be much smaller than the
³³⁴ first azimuthal derivative. Besides, the rotation speed contained in $\dot{n}$ can also raise the value by one
³³⁵ order of magnitude.

³³⁶ *4.3. Unsteady case with permeable FW-H approach*

³³⁷ In this section, the acoustic pressure is calculated with the FW-H permeable surface. The wake
³³⁸ sheet length is set to 3 revolutions for the study in this section.
³³⁹ Without using the virtual source correction, we have firstly studied the sensitivity of the acoustic
³⁴⁰ pressure to the permeable surface size. Four different cylindrical permeable surfaces have been studied.
³⁴¹ They are denoted with the names *basic*, *small*, *large*, and *long*, respectively. Their size and discretization
³⁴² parameters are listed in table 2 and depicted in Figure 11. The adopted panel sizes are chosen through
³⁴³ mesh independence study for every permeable surface so that the mesh convergence is achieved.
³⁴⁴ Generally, when the permeable surface is small, it is located near to the potential boundaries (blades
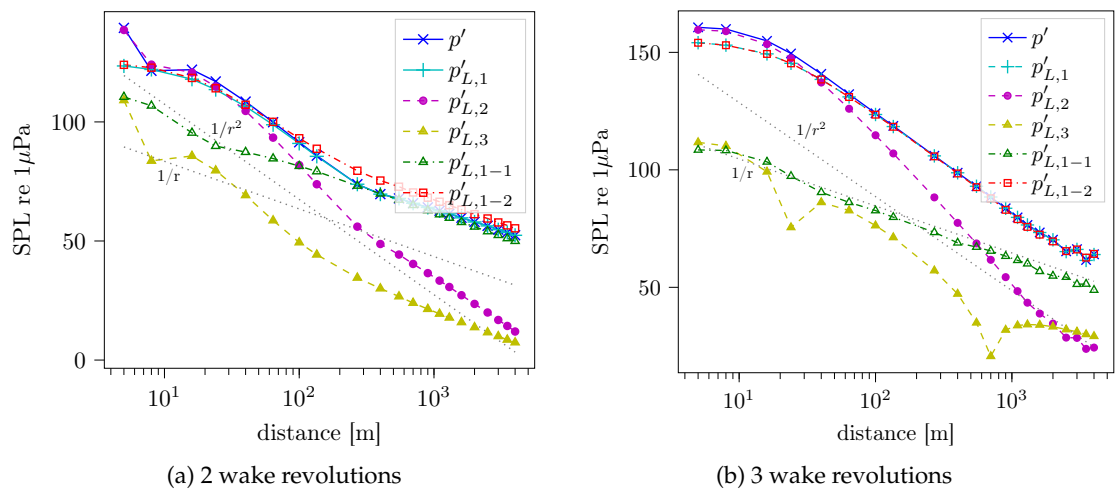
(a) 2 wake revolutions

(b) 3 wake revolutions

Figure 10. Contribution of different FW-H terms in the wake induced SPL. The loading terms $p'_{L,1-1}$ and $p'_{L,1-2}$ are defined in the equations (27) and (28).
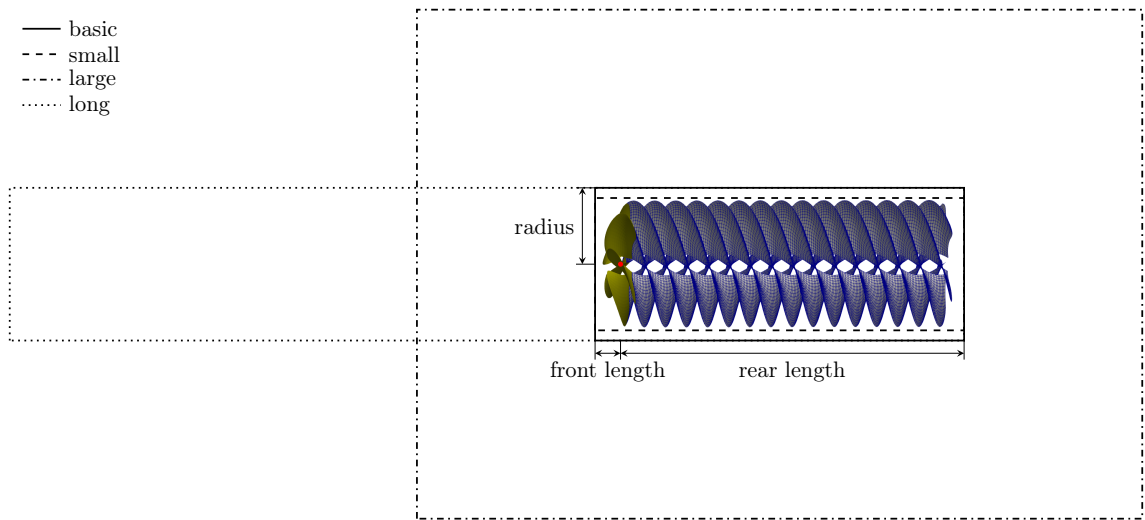

Figure 11. Different permeable surfaces and the size parameters. The size parameters are depicted on the *basic* permeable surface. Three wake revolutions are shown here.

345 and wake sheets), so the mesh on it should be fine to capture the flow field variation correctly. When
346 the permeable surface is large, the mesh can be relatively rough due to the smooth flow field.

Table 2. Size and discretization parameters for the permeable surfaces with names *basic*, *small*, *long*, and *large*. The meaning of size parameters are explained in Figure 11.

parameters	basic	small	long	large
front length	1.5m	1.5m	50m	13m
rear length	21.5m	21.5m	21.5m	33m
radius	0.6D	0.52D	0.6D	2D
panel size	1m	0.2m	1m	2m

347 Figure 12 shows the results obtained with the permeable surfaces listed in table 2. The results
348 correlate well with each other. The first two observer points are located inside the large permeable
349 surface, so the results show some anomaly. The SPL variations show the same tendency with those
350 obtained using the direct FW-H method in section 4.2, but an underestimation can be observed in the
351 range inside 200m. Larger permeable surface leads to more underestimation, however, the difference
352 is quite small. The permeable surface results achieve the r^{-1} decay rate much earlier than the direct
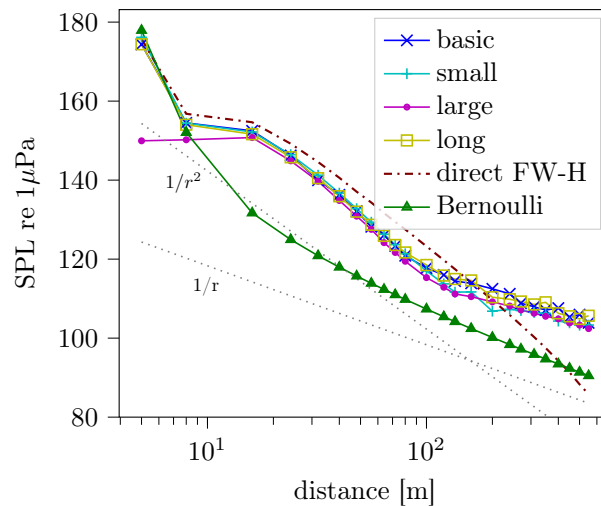353 FW-H method. This results in an overestimation of SPL beyond 200m. Later we would see that this

Figure 12. SPL variations obtained with permeable surfaces having different sizes. Direct FW-H means the calculation with blade surface and wake surface as in section 4.2.

premature arrival of the r^{-1} decay rate is caused by the non-vanishing potential source inside the permeable surface and can be solved by the virtual source correction.

Figure 13 shows the contributions of different FW-H terms on the *basic* permeable surface, with and without consideration of the ship wake velocity. The first thickness term $p'_{T,1}$ is always dominant. As explained in section 2.4, with the current configuration the term $p'_{T,1}$ is not influenced by the ship wake velocity. If we compare $p'_{T,2}$ and $p'_{T,2}$ in both cases, small influences of the ship wake field can be observed in the range between 20m and 100m. However, all the other terms are secondary when compared to $p'_{T,1}$. Thus, whether to include the ship wake velocity on the permeable surface would have no obvious influence on the final acoustic results. In the following study, the ship wake velocity will not be considered on the permeable surface.
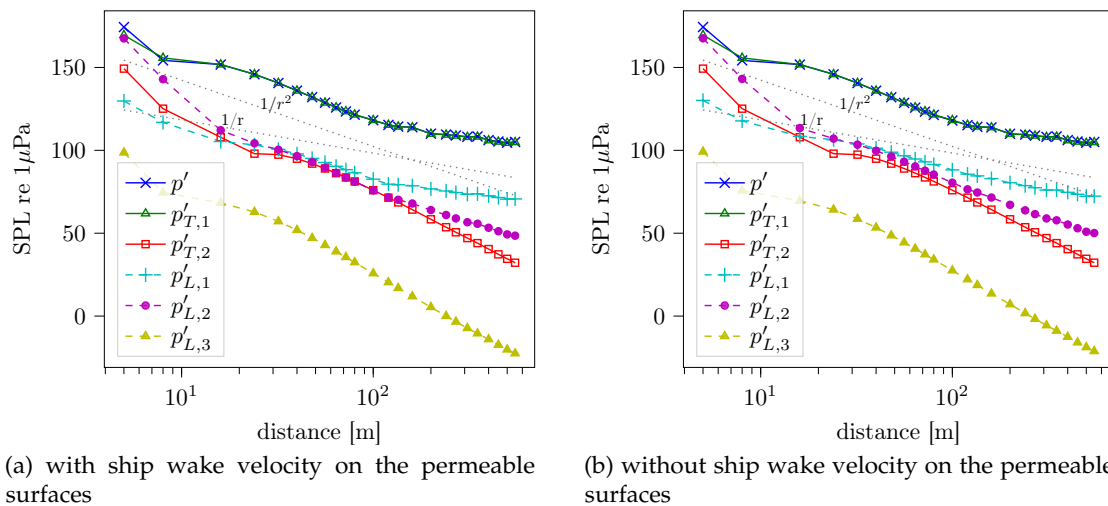

(a) with ship wake velocity on the permeable surfaces

(b) without ship wake velocity on the permeable surfaces

Figure 13. The influence of whether including the ship wake velocity on the permeable surfaces. Contributions of different FW-H terms on the permeable surfaces are plotted.

Then we come back to the premature arrival of the r^{-1} decay rate shown in Figure 12. According to the analysis in section 2.4, due to the use of 2D ship wake velocity information as a 3D velocity field in BEM, the potential source on the propeller surface do not integrate to zero. This leads to a non-physical fictitious volume flux on the permeable surface. The sound pressure amplitude induced by the volume flux (like a monopole) decays as r^{-1}. When it dominates the acoustic pressure field, the

total SP would have a decay rate of r^{-1}. Figure 14 shows the timely variation of the integral potential source on propeller surface and the volume flux on the permeable surface, i.e.

$$\int_{S_B} \sigma dS \quad and \quad \int_{f=0} (u_n + v_n) dS \tag{36}$$

364 with S_B being the propeller surface, and $f = 0$ denoting the FW-H permeable surface. The volume flux
365 without any correction equals to the integral source strength. Its absolute value can be up to 0.4m³ and
366 the oscillation amplitude is more than 0.2m³. With the virtual source correction method described in
367 section 2.4, the volume flux decreases obviously. The absolute value and oscillation amplitude of the
368 corrected volume flux would depend on the size and discretization of the permeable surface. For the
369 *large* permeable surface they are 2e-3m³ and 2e-4m³, respectively. For the *basic* one they are 0.015m³
370 and 0.02m³, respectively. Generally, larger permeable surface and finer discretization lead to smaller
371 volume flux. Figure 15 shows the SPL obtained with and without the virtual source correction, using
372 the basic permeable surface. An improvement for almost the whole distance range can be observed.
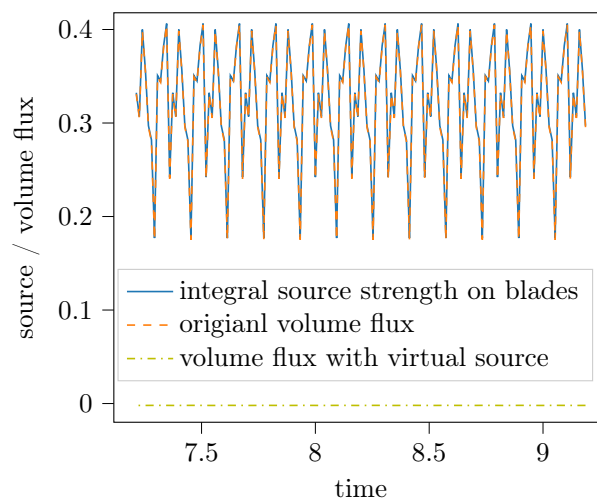

Figure 14. The total potential source strength inside the permeable surface and the volume flux on the *large* permeable surface.
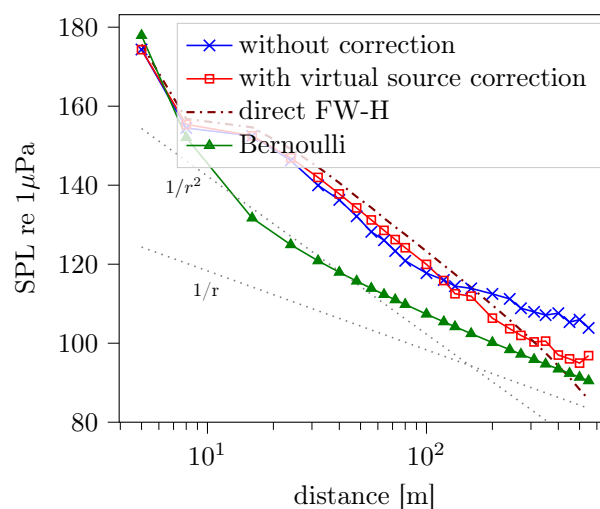

Figure 15. The SPL variation obtained using the *basic* permeable surface with and without virtual source correction.

With the virtual source correction, the influence of the permeable surface size is restudied for both the 1st and 3rd BPF. The results are given in Figure 16. When compared to the direct FW-H results, a general underestimation can be observed. Larger permeable surfaces have more underestimation. The underestimation is more obvious for the higher frequency. This is because the wavelength is shorter, and then the phase difference due to the incompressible assumption inside the permeable surface becomes more significant. At the distance 100m, the underestimations for the 1st BPF are around 3dB with the small and 4.5dB with the large permeable surface. For the 3rd BPF, they are around 1.5dB and 7dB respectively. The anomaly beyond 300m shown in Figure 16 might be due to the remaining numerical volume flux.
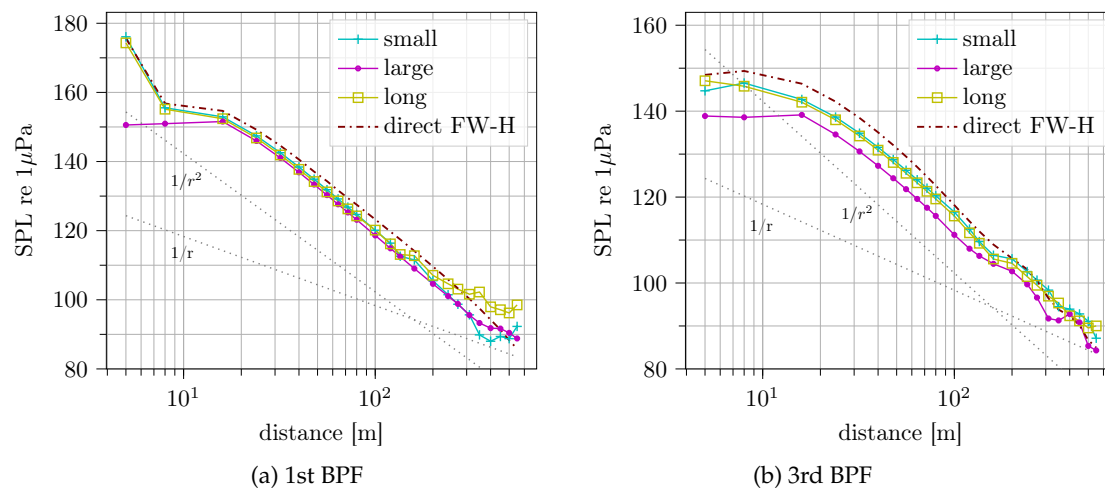

Figure 16. SPL variations obtained with permeable surfaces having different sizes. The virtual source correction is used.

5. Discussions and Conclusions

The property of the sound field calculated with FW-H equation for non-cavitating propeller as well as the property of different FW-H terms are studied with the potential BEM (Boundary Element Method) approach, taking its advantage of zero numerical diffusion and the lack of spatial vorticity distribution, which could be hard to be handled correctly.

Firstly, it is found that the sound field of the open water case and the unsteady case have totally different properties. In the open water case, the thickness terms are dominant and the SP (Sound Pressure) has a very fast decay rate in the relative near field (up to 100m for the studied case). In the unsteady case, the thickness terms are negligible when compared to the loading terms. The fast decay ends within two propeller diameters.

The potential propeller wake sheet, which models the shedding vorticity, has an important contribution to the acoustic pressure in the unsteady case. It can be the dominant sound source within the distance up to several kilometres. Obvious dependence on the extension of the wake sheet has been observed. Normally in BEM, the length of the wake sheet is chosen according to the convergence of hydrodynamic forces on the blades. For the acoustic simulation, a more physical consideration is necessary, e.g. considering the diffusion process or the stability of the vortex structures.

In the unsteady case, the dominant terms on the blade surface and the wake sheet are both the first loading term in Farassat 1A formula, which contains the pressure's time derivative. They are both related to the azimuthal derivative of the ship wake velocity. Thus, a precise description of the ship wake field regarding the azimuthal continuity and variation is a prerequisite for the correct acoustic pressure prediction.

The way to use ship wake field in BEM, i.e. using the velocities on a 2D plane as a 3D distribution, produces a non-divergence-free velocity field. This leads to a non-vanishing integral source strength

on the blade surface, which produces a fictitious volume flux when the permeable FW-H approach is used. A virtual source correction method is proposed to cancel out such a numerical volume flux. The proposed method is quite simple and proved to work very well.

With the permeable FW-H approach, the thickness term is dominant. The term with the time derivative of normal velocity is especially important. It is also found that the permeable FW-H always produces an underestimation, which is around 3dB for the BPF (Blade Pass Frequency) and becomes severer for higher frequencies. A larger permeable surface leads to further underestimation. This might be due to the ignoring of sound travel time inside the permeable surface.

It needs to be emphasized that the formula to consider the acoustic contribution of the propeller wake sheet is proposed for the first time. The good correlation between the direct FW-H result and permeable FW-H result verifies the correctness of the proposed formula.

Acknowledgments

References

1. Krasilnikov, V. CFD modeling of hydroacoustic performance of marine propellers: Predicting propeller cavitation. Proceedings of the 22nd Numerical Towing Tank Symposium; , 2019.

2. European-Commission. Our Oceans, Seas and Coasts, 2019. accessed on: 2020-07-31.

3. AQUO Project Consortium. AQUO: Achieve Quieter Oceans by shipping noise footprint reduction, 2012. accessed on: 2020-07-31.

4. SONIC Project Consortium. SONIC: Supression Of Underwater Noise Induced by Cavitation, 2015. accessed on: 2020-08-31.

5. ProNoVi-Consortium. ProNoVi:Analysis Methods and Design Measures for the Reduction of Noise and Vibration Induced by Marine Propellers, 2017. accessed on: 2020-07-31.

6. Williams, J.F.; Hawkings, D.L. Sound generation by turbulence and surfaces in arbitrary motion. *Phil. Trans. R. Soc. Lond. A* **1969**, *264*, 321–342.

7. Farassat, F. Derivation of Formulations 1 and 1A of Farassat. Technical Report NASA/TM-2007-214853, NASA, Langley Research Center, Hampton, Virginia, USA, 2007.

8. Ianniello, S.; Muscari, R.; Di Mascio, A. Ship underwater noise assessment by the Acoustic Analogy part II: hydroacoustic analysis of a ship scaled model. *Journal of marine Science and technology* **2014**, *19*, 52–74.

9. Lidtke, A.K.; Humphrey, V.F.; Turnock, S.R. Feasibility study into a computational approach for marine propeller noise and cavitation modelling. *Ocean Engineering* **2016**, *120*, 152–159.

10. Li, D.Q.; Hallander, J.; Johansson, T. Predicting underwater radiated noise of a full scale ship with model testing and numerical methods. *Ocean Engineering* **2018**, *161*, 121–135.

11. Bensow, R.; Liefvendahl, M. An acoustic analogy and scale-resolving flow simulation methodology for the prediction of propeller radiated noise. 31th Symposium on Naval Hydrodynamics; , 2016.

12. Göttsche, U.; Lampe, T.; Scharf, M.; Abdel-Maksoud, M. Evaluation of Underwater Sound Propagation of a Catamaran with Cavitating Propellers. Proceedings of the 6th International Symposium on Marine Propulsors (SMP'19); , 2019.

13. Seol, H.; Suh, J.C.; Lee, S. Development of hybrid method for the prediction of underwater propeller noise. *Journal of Sound and Vibration* **2005**, *288*, 345–360.

14. Ianniello, S. The Ffowcs Williams–Hawkings equation for hydroacoustic analysis of rotating blades. Part 1. The rotpole. *Journal of Fluid Mechanics* **2016**, *797*, 345–388.

15. Cianferra, M. Acoustic Analogies and Large-Eddy Simulations of Incompressible and Cavitating Flows Around Bluff Bodies. PhD thesis, Università degli Studi di Trieste, 2018.

16. Liefvendahl, M.; Bensow, R. Simulation-Based Analysis of Flow-Generated Noise from Cylinders with Different Cross-Sections. 32nd Symposium on Naval Hydrodynamics; , 2018.

17. Wang, Y.; Göttsche, U.; Abdel-Maksoud, M.; Krüger, S. Different techniques to simulate tandem propeller with boundary element method. 11th internationa workshop on ship and marine hydrodynamic; , 2019.

18. Wang, Y.; Abdel-Maksoud, M.; Song, B. A fast method to realize the pressure Kutta condition in boundary element method for lifting bodies. *Ocean Engineering* **2017**, *130*, 398–406. doi:10.1016/j.oceaneng.2016.12.009.

19. Katz, J.; Plotkin, A. *Low-speed aerodynamics*; Vol. 13, *Cambridge Aerospace Series*, Cambridge University Press: Cambridge, United Kingdom, 2001.

20. Wang, Y.; Abdel-Maksoud, M.; Song, B. Convergence of different wake alignment methods in a panel code for steady-state flows. *Journal of Marine Science and Technology* **2016**, *21*, 567–578. doi:10.1007/s00773-016-0375-0.

21. Bres, G.; Pérot, F.; Freed, D. A Ffowcs Williams-Hawkings solver for Lattice-Boltzmann based computational aeroacoustics. 16th AIAA/CEAS aeroacoustics conference, 2010, p. 3711.

22. MOERI. MOERI Container Ship (KCS), 2008. accessed on: 2015-9-14.